J Nanostruct 16(2): 1800-1812, Spring 2026

RESEARCH PAPER

Simple Synthesis of ZnS/Chitosan and HgS/Chitosan Nanocomposites as Absorbents for Removing Water-Soluble Organic-Pollutants

Azam Sobhani [1]*, *Shaghayegh Sharifan* [2]

[1] *Department of Chemistry, Kosar University of Bojnord, Bojnord, 94531–55168, Republic of Iran*

[2] *Department of Chemistry, Faculty of chemistry, Semnan university, Semnan, Iran*

ARTICLE INFO

Article History:
Received 08 December 2025
Accepted 17 March 2026
Published 01 April 2026

Keywords:
Chitosan
Dye removal
Mercury sulfide
Nanocomposite
Zinc sulfide

ABSTRACT

In the present study, MS nanostructures (MS NSs), and MS/chitosan nanocomposites (MS/Chit NCs) were synthesized, M= Zn, Hg. First, [M(Tu)] complex was synthesized by a simple reflux route. In the next step, MS nanostructures were prepared by thermal decomposition of [M(Tu)] precursors at 500 ˚C for 4h. Then MS/Chit NCs were synthesized. The products were characterized by XRD, SEM, EDS, FT-IR and the effect of the surfactant was investigated. XRD confirmed formation of MS NSs and MS/Chit NCs. SEM images showed morphology of the products. Finally, the application of nanocomposites as absorbents for removing organic dyes from water was studied. Two dyes were used, including methyl orange (MO) and methylene blue (MB). The absorption spectra results indicated the suitable performance of ZnS NSs in MO removal and ZnS/Chit NCs in MB removal. Water contains organic dyes which cause a potential hazard to the environment hence these dyes need to remove from the water bodies.

How to cite this article
Sobhani A., Sharifan S. Simple Synthesis of ZnS/Chitosan and HgS/Chitosan Nanocomposites as Absorbents for Removing Water-Soluble Organic-Pollutants. J Nanostruct, 2026; 16(2):1800-1812. DOI: 10.22052/JNS.2026.02.031

INTRODUCTION

Zinc sulfide (ZnS) and mercury sulfide (HgS) are important semiconductor materials with applications in optoelectronics, photocatalysis, and biomedical imaging [1]. Various synthetic methods have been developed to control their phase composition, morphology, and optical properties. ZnS exists in two main crystalline forms: cubic zinc blende (sphalerite) and hexagonal wurtzite. Researchers have employed multiple approaches for its synthesis, including solid state reaction, chemical precipitation, solvothermal, chemical vapor deposition [2-5]. HgS exists in two primary phases: red α-HgS (cinnabar) and black β-HgS (metacinnabar) [6]. Different synthetic strategies have been explored for this material, including direct combination, aqueous precipitation, solvothermal, biomimetic synthesis [7-11].

Increasing industrial development and growing population have led to an increase in organic dyes in water. These can pose environmental problems such as soil, water and air contamination [12-15]. The water contamination problem has become a significant concern in recent years. The organic dyes reduce the dissolved oxygen level in water and prevent sunlight from entering the water sources. Thus, dye removal from water is essentially important [16-18]. Several strategies to

* *Corresponding Author Email: sobhani@kub.ac.ir*

remove organic contamination from the aqueous system have been developed, including adsorption [19], electrocatalysts [20, 21], and photocatalysts [22, 23].

Currently, the use of proteins and polysaccharides (natural polymers) are broadly developed. Polysaccharides are a large group of biopolymers with interesting properties. Chitosan is a polysaccharide bioresource found in some fungi, worms, diatoms, mollusks, and sponges. Chitosan is an abundant and natural polymer. Much attention has been paid to the synthesis of the nanocomposites with chitosan due to valuable properties, applications in nanotechnology area, etc [24-26]. Chitosan and its nanocomposites are excellent candidates to use as absorbent, photocatalyst, etc. [27]. In this work, we synthesize ZnS/Chit and HgS/Chit NCs and use them as absorbent for the MO and MB removal. However, research on the application of ZnS/Chit and HgS/Chit NCs as absorbents for dye removal remains limited. Despite the inherent toxicity associated with mercury-based compounds, HgS was deliberately selected in this work owing to its distinctive optical and electronic characteristics, its thermodynamic stability among mercury species, and its relevance as a model system for investigating the synthesis and properties of II–VI semiconductor sulfides. Furthermore, the incorporation of HgS into composite structures offers a promising platform to explore advanced functionalities such as enhanced photocatalytic activity, charge-transfer processes, and high-performance sensing applications. This research is the first study comparing the synthesis of ZnS, HgS, ZnS/Chit and HgS/Chit NCs under different conditions and comparing their application for removing MO and MB from aqueous solutions.

MATERIALS AND METHODS

Materials and Characterization

$Ni(NO_3)_2.6H_2O$, $Hg(NO_3)_2.H_2O$ and thiourea ($H_2N–C(=O)–NH_2$) were provided from Merck. XRD (X-ray diffraction) patterns were studied by a Philips X'pertPro diffractometer with Ni-filtered Cu Kα radiation and λ = 1.54 Å. The morphology and EDS (energy-dispersive X-ray spectroscopy) spectrum of the samples were studied by TESCAN Mira3 FE-SEM, field emission scanning electron microscope (scanning electron microscopy). The FT-IR (Fourier transform infrared) and UV-Vis spectra of the products were studied by spectrophotometers made in the American Thermo scientific company, Nicolet IS 10 and Evolution 300 spectrophotometers, respectively.

Preparation of [M(tu)] precursor

First, 2 mmol metal nitrate salt was dissolved in distilled water, surfactant (CTAB, PVA and PEG) was added to the solution and it refluxed at 120° C. After 1h, thiourea solution (2 mmol) was added, then the mixture was refluxed at 120° C for 1h. With evaporation of the solution, a solid was recovered, filtered, washed with distilled water and ethanol

Table 1. The reaction conditions for the synthesis of MS NSs and MS/Chit NCs in this work.

Sample no.	Precursors	Surfactant	T and t of thermal decomposition
1	$Zn(NO_3)_2.6H_2O$ + Tu	CTAB	500 ˚C, 4 h
2	$Zn(NO_3)_2.6H_2O$ + Tu	PVA	500 ˚C, 4 h
3	$Zn(NO_3)_2.6H_2O$ + Tu	PEG	500 ˚C, 4 h
4	$Zn(NO_3)_2.6H_2O$ + Tu	–	500 ˚C, 4 h
5	Sample 1 + chitosan	–	–
6	Sample 2 + chitosan	–	–
7	Sample 3 + chitosan	–	–
8	Sample 4 + chitosan	–	–
9	$Hg(NO_3)_2.H_2O$ + Tu	CTAB	500 ˚C, 4 h
10	$Hg(NO_3)_2.H_2O$ + Tu	PVA	500 ˚C, 4 h
11	$Hg(NO_3)_2.H_2O$ + Tu	PEG	500 ˚C, 4 h
12	$Hg(NO_3)_2.H_2O$ + Tu	–	500 ˚C, 4 h
13	Sample 9 + chitosan	–	–
14	Sample 10 + chitosan	–	–
15	Sample 11 + chitosan	–	–
16	Sample 12 + chitosan	–	–

T = Temperature, t = time

and dried.

Preparation of MS NSs

[M(Tu)] complex was decomposed in a furnace at 500 ˚C for 4h, and zinc sulfide, mercury sulfide nanostructures were parepared.

Preparation of MS/Chit NCs

The chitosan was dissolved with distilled water and acetic acid. In the next step, a solution was

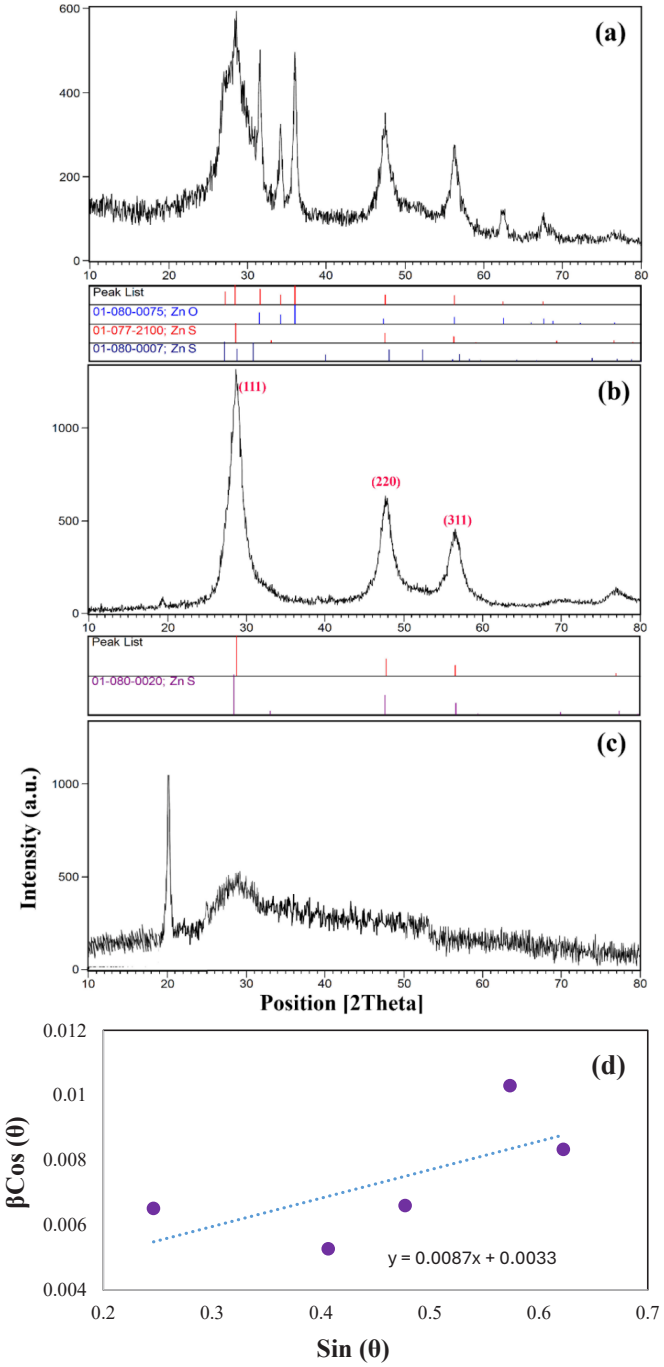

Fig. 1. XRD patterns of ZnS NSs and ZnS/Chit NCs: (a) sample 1, (b) sample 4, (c) sample 8 and (d) Williamson-Hall plot for sample 4.

prepared containing a ratio of 1:1 chitosan and MS. The solution was stirred for 24h, washed with ethanol, then dried in furnace under vacuum. The different conditions for synthesizing MS NSs and MS/Chit NCs have been summarized in Table 1.

Application

The MS/Chit NCs were applied for the MB and MO removal from aqueous solutions. A solution of dye with 10^{-4} ML^{-1} concentration was prepared. Some of this solution (50 ml) was added in a beaker containing 10 mg of the nanocomposite. The mixture was stirred for 30 min at room temperature. The UV-Vis spectra of this mixture and also pure MB solution were taken and the adsorption capacity of the MS/Chit NCs over MB and MO dyes evaluated. The photocatalytic capabilities of the products were examined using photodegradation of 100 ml of MB and MO, when exposed to simulated sunlight in a laboratory. The combination of 70 mg of the photocatalyst in 100 ml of the dye solution with deionized water was subjected to magnetic stirring for 30 min in darkness to establish an adsorption/desorption balance between dye molecules and photocatalyst before photodegradation reactions [28]. For reactions involving photodegradation, the light source was exposed to radiation on samples for a specific duration (90 min), and the irradiated solutions were centrifuged and gathered. The level of dyes was measured using a spectrophotometer. The UV–Vis absorbance of each dye solution was recorded at its characteristic maximum absorbance wavelength (λ_{max}) [29]. The photodegradation percentage was calculated using the below equation (Eq. 1):

$$D\% = 1-(A_t/A_0) \times 100 \quad (1)$$

Where D% introduces degradation percent of the dye, A_0 and A_t introduce the absorbance values at starting and t min.

RESULTS AND DISCUSSION

Characterization of ZnS NSs and ZnS/Chit NCs

The structural observations and phase purity of

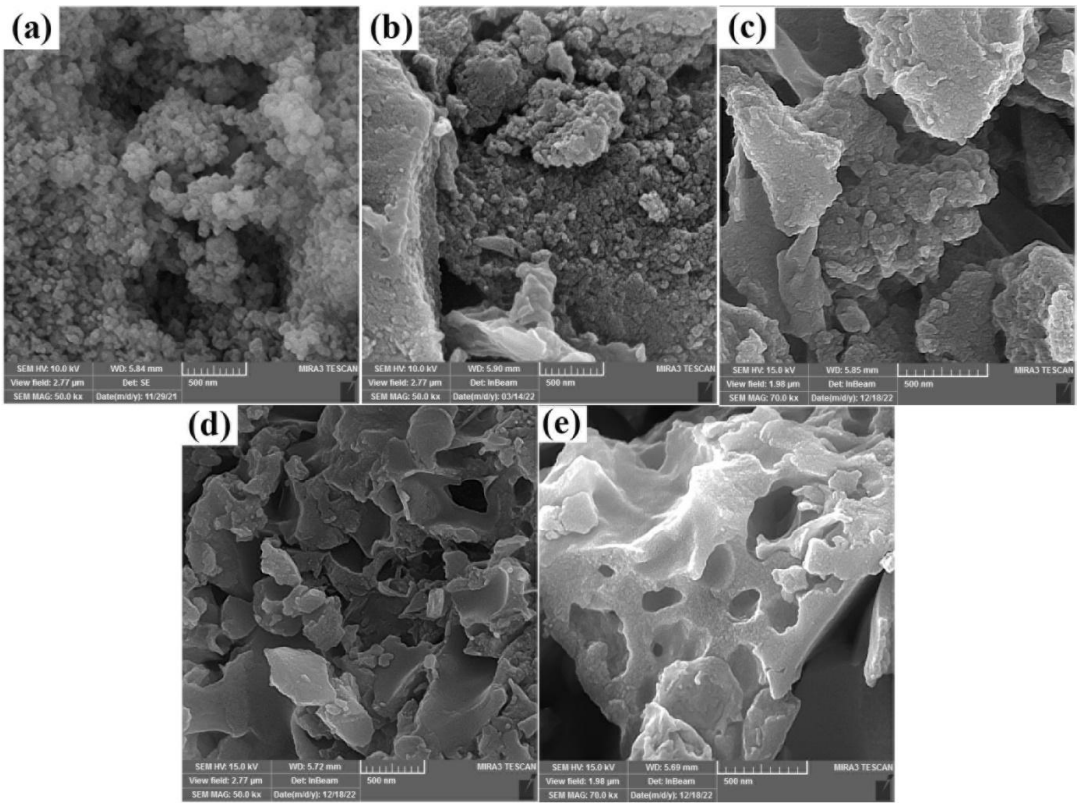

Fig. 2. SEM images of: (a) ZnS NSs (sample 4), (b, c, d, e) ZnS/Chit NCs, samples 8, 5, 6 and 7, respectively.

the samples confirm with XRD patterns. In Fig. 1 the XRD patterns of ZnS NSs and NCs have been illustrated. As well as seen, employing CTAB as surfactant (sample 1), both ZnS and ZnO are formed. However, in the absence of surfactant (sample 4), pure ZnS with JCPDS card number 01-080-0020 is formed, as shown in Fig. 1a and b, respectively. The XRD pattern of the product (sample 4) stirred for 24 h with chitosan shows the peaks of both chitosan and ZnS in XRD pattern in Fig. 1c, confirming the formation of the nanocomposite. The XRD pattern of chitosan exhibits characteristic broad peaks at approximately 2θ = 10° and 20°, attributed to its hydrated crystalline structure [30]. Fig. 1c shows that these peaks overlap with ZnS peaks in the ZnS/Chit NC, confirming successful integration.

The sample crystallite size (D) was determined by applying Scherrer equation (Eq. 2):

$$D = K\lambda/\beta Cos\theta \quad (2)$$

In accordance with Eq. (2), λ indicates the X-ray wavelength (1.54 A°), β expresses the FWHM value, and K displays the Bragg constant (0.9). For sample 4, crystallite size was determined to be approximately 20 nm using this equation.

Crystallinity percentage was considered *via* Eq. 3, as follows [31]:

$$\text{Crystallinity } \% = A_c / (A_c + A_a) \times 100 \quad (3)$$

Where A_c is area under crystalline peaks and A_a is area of the amorphous background. Percentage of crystallinity for ZnS was calculated to be 76 %.

Also, crystallite size calculated using Williamson-hall plot for studying the microstructural properties [32]. By plotting βcosθ versus sinθ, we may ascertain the crystallite size (Kλ/D = intercept) and the strain component from the slope (Fig. 1d). The derived results in Fig. 1d demonstrate that, for sample 4, non-zero residual tension causes the crystallite size determined by the Scherer equation (D ~ 20 nm) to be less than the crystallite size determined by the Williamson-Hall plots (D = 42 nm).

Fig. 2 shows SEM images of ZnS NSs (sample 4) and ZnS NCs. Thees images were taken to investigate the morphology of the synthesized products. SEM images in Fig. 2a are related to the sample prepared without surfactant and confirm the formation of ZnS nanoparticles with even diameters and about 20 nm that are

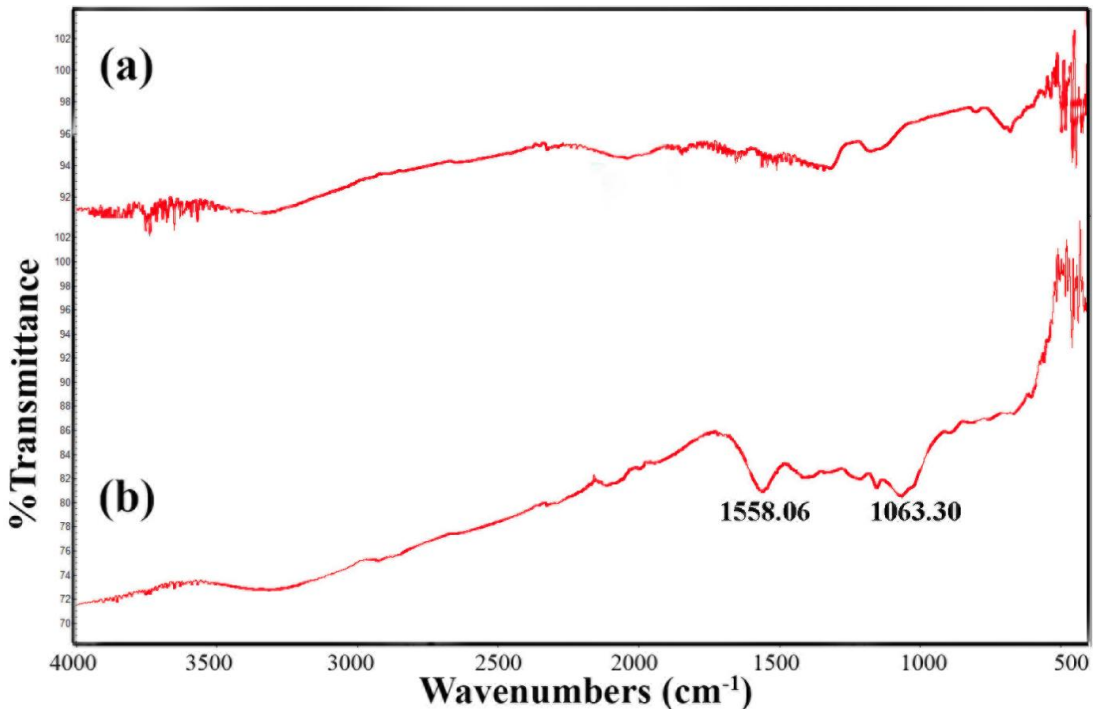

Fig. 3. FT-IR spectra of: (a) ZnS NSs (sample 4) and (b) ZnS/Chit NCs (sample 7).

agglomerated. Fig. 2 b-e shows SEM images of ZnS/Chit NCs obtained from zinc sulfides synthesized under various conditions. SEM images in Fig. 2b and c show ZnS nanoparticles embedded within chitosan, which confirms the formation of the nanocomposite. These images show that sample 8 (Fig. 2b) has a smaller particle size and uniform particle distribution than sample 5 (Fig. 2c). In SEM images of samples 6 and 7, which are shown in Fig. 2d and e, the aggregated and bulk structures are observed that are related to chitosan. There is no effect of ZnS nanoparticles in these images; therefore, as a result of the SEM images, we select sample 8 as the optimum nanocomposite.

As depicted in Fig. 3, the FT-IR spectra were utilized to investigate the functional groups in the samples. The ZnS NSs spectrum shows a short peak at about 700 cm^{-1}, which is associated with the vibrational mode of Zn-S. For ZnS/Chit NCs, the wide band observed at about 3300 cm^{-1} results from the overlapping O-H and N-H stretching vibrations in chitosan, while the band at 1558.06 cm^{-1} is attributed to the CO stretching modes associated with the acetylated groups in chitosan. The peaks observed at about 1063 cm^{-1} correspond to the C–O stretching of primary alcoholic groups in chitosan. The peak at about 1400 cm^{-1} can be attributed to the CH_3 deformation present in the structure of chitosan [33]. These observations along with XRD and EDS results further confirm the purity of samples.

The EDS determines the elemental composition of materials. Fig. 4 depicts the EDS spectrum of ZnS NSs. This figure shows Zn and S elements and confirms the formation of zinc sulfide nanostructures.

Characterization of HgS NSs and HgS/Chit NCs

The XRD patterns in Fig. 5a are related to sample 11 prepared with PEG and matched to the diffraction peaks of pure HgS of JCPDS card number 00-002-0453, without the formation of any impurity. After stirring the HgS solution for 24h with chitosan, HgS/Chit NC was prepared. The XRD pattern of this nanocomposite shows characteristic peaks of both HgS and chitosan with reduced intensities in Fig. 5b, confirming the formation of the nanocomposite. Shifting of peaks in both directions, decrease in their intensity, and disappearance of some peaks can be observed after formation of the nanocomposites in this figure.

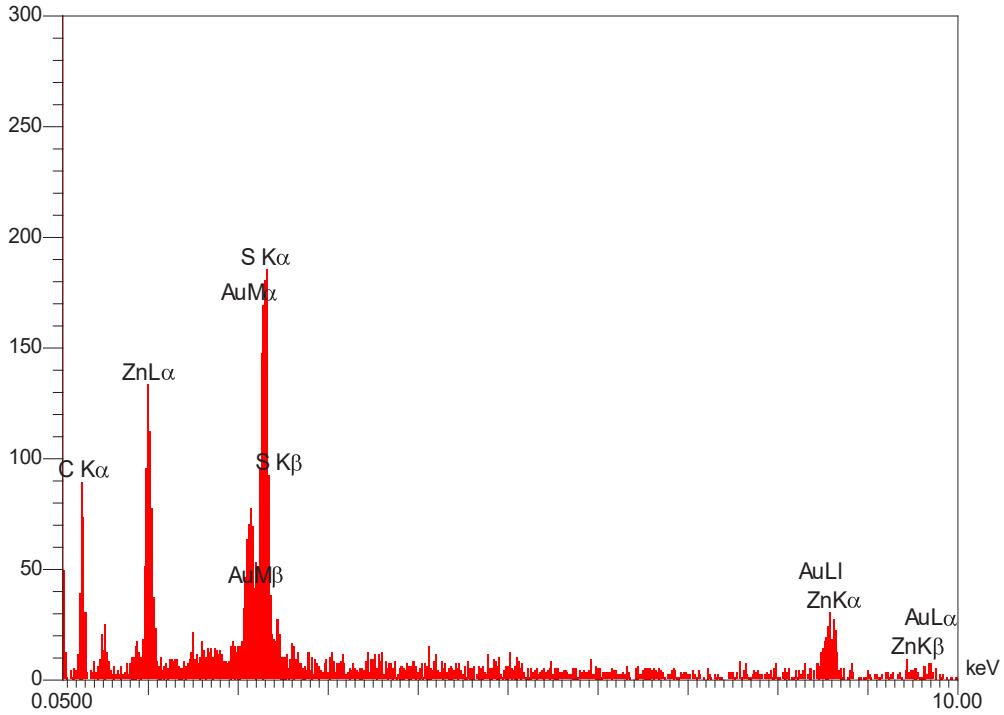

Fig. 4. EDS pattern of ZnS NSs (sample 3).

The crystallite size was calculated using the Scherrer equation for sample 11, and the obtained value was approximately 71 nm, which clearly demonstrates the nanoscale nature of the crystallites in this sample. Also, in the case of sample 11, the crystallite size was calculated using the Williamson-Hall formula (77 nm). Fig. 5c illustrates the almost zero slope of sample 11. This

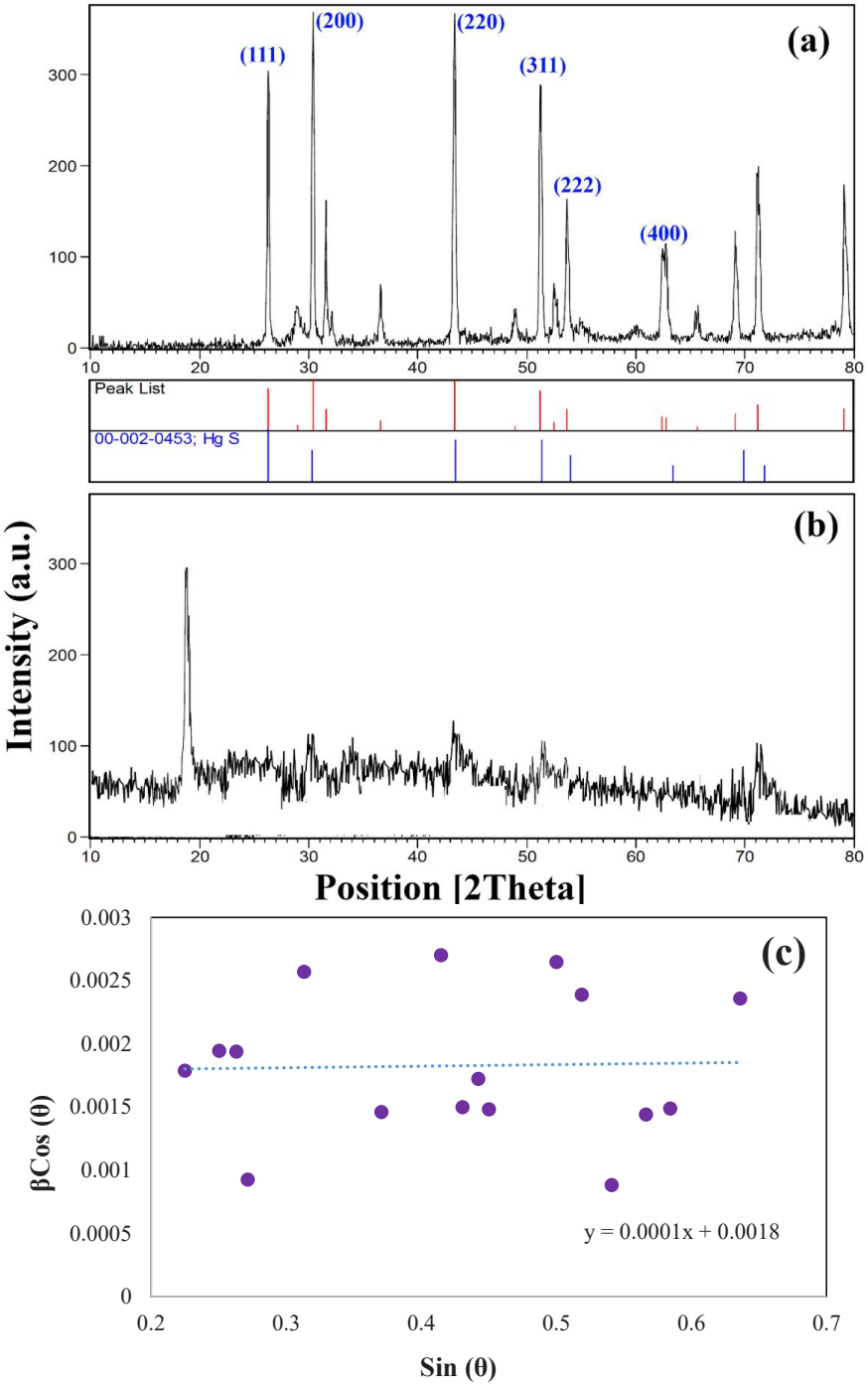

Fig. 5. XRD patterns of: (a) HgS NSs (sample 11), (b) HgS/Chit NCs (sample 15) and (c) Williamson-Hall plot for sample 11.

supports the Williamson-Hall formula's and the Scherrer equation's findings of the same crystallite sizes.

Additionally, Fig. 6 displays SEM images of HgS NSs and HgS/Chit NCs. In Fig. 6a, HgS nanoparticles with diameters below 50 nm are observed, though they exhibit agglomeration. Analysis of the SEM images and morphological studies of the HgS/Chit NCs reveals homogeneous distribution and good dispersion of nanoparticles within the chitosan matrix. However, some degree of agglomeration is evident in Fig. 6b-e, likely due to reduced crystallinity and an increased amorphous phase.

Fig. 7 shows a schematic diagram for ZnS, HgS, and ZnS/Chit and HgS/Chit NCs with SEM images

Mechanism of metal sulfide nanostructure formation

The mechanism for the formation of metal sulfide nanostructures is proposed as follows.

$$M^{2+}\ (Zn^{2+}\ /\ Hg^{2+}) + nCS(NH_2)_2 \rightarrow [M(CS(NH_2)_2)_n]^{2+}$$

$$CS(NH_2)_2 \xrightarrow{\Delta} H_2S + HNCS$$

$$CS(NH_2)_2 \xrightarrow{\Delta} HSCN + H_2$$

$$H_2S \rightarrow 2H^+ + S^{2-}$$

$$HSCN \xrightarrow{\Delta} H^+ + SCN^- \xrightarrow{\Delta} S^{2-} + CN^-$$

$$M^{2+} + S^{2-} \xrightarrow{\Delta} MS\ (s)\ (ZnS/HgS)$$

Applications of the products in dye removal

The UV-Vis absorbance spectra of the pure MO, and MO adsorbed on the surface of the nanostructures and nanocomposites as-prepared in this work, have been shown in Fig. 8. The black curve in this figure corresponds to the UV-Vis spectrum of MO. The results demonstrate that ZnS NS acts as an effective adsorbent for MO removal from aqueous solutions, as evidenced by the complete elimination of MO's UV-Vis peaks in

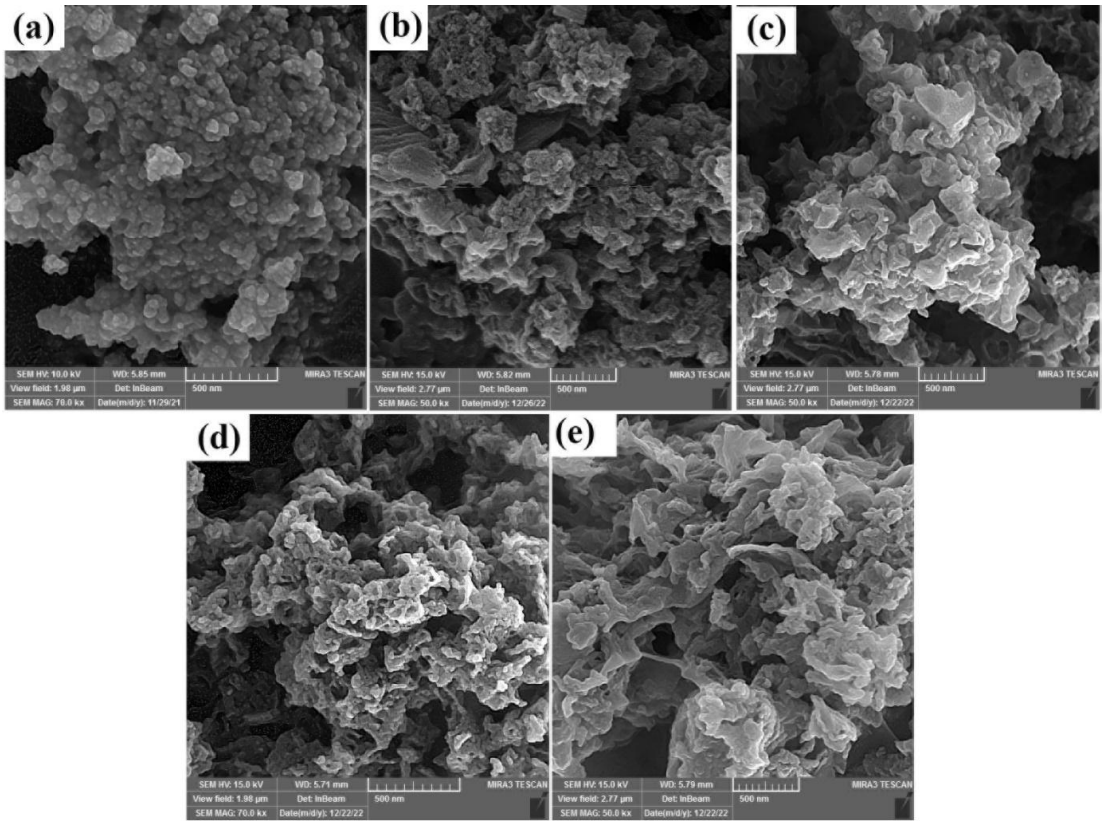

Fig. 6. SEM images of: (a) HgS NSs (sample 10), (b, c, d, e) HgS/Chit NCs, samples 14, 13, 15 and 16, respectively.

Fig. 8a. In contrast, neither ZnS/Chit nor HgS/Chit shows significant adsorption capability for MO degradation. Fig. 8b illustrates the degradation efficiency of MO in the presence of ZnS, ZnS/Chit, and HgS/Chit. The among the synthesized products, ZnS exhibits the highest photocatalytic activity toward the degradation of MO. Accordingly, to investigate the photocatalytic performance, ZnS was employed as a photocatalyst for the degradation of MO. Fig. 8c demonstrates the influence of MO concentration on the degradation efficiency. Various concentrations of MO were examined to evaluate its photodegradation in order to enhance the photodegradation process. In Fig. 8c, as the concentration of MO rose from 5 ppm to 15 ppm, the photodegradation rate fell from 79 % to 32 %. The information indicates that a higher initial concentration of dye makes it more challenging to decompose. Using more dye results in a greater amount sticking to the catalyst's surface. This complexity impairs the catalyst's ability to absorb light and generate the necessary energy for decomposing the dye, leading to diminished efficiency in its cleaning action. Additionally, when there is a higher concentration of dye, the light must penetrate deeper into the dye solution. For optimal results from ZnS, the ideal concentration of MO is 5 ppm.

The UV-Vis absorbance spectra of the pure MB, and MB adsorbed on the surface of the

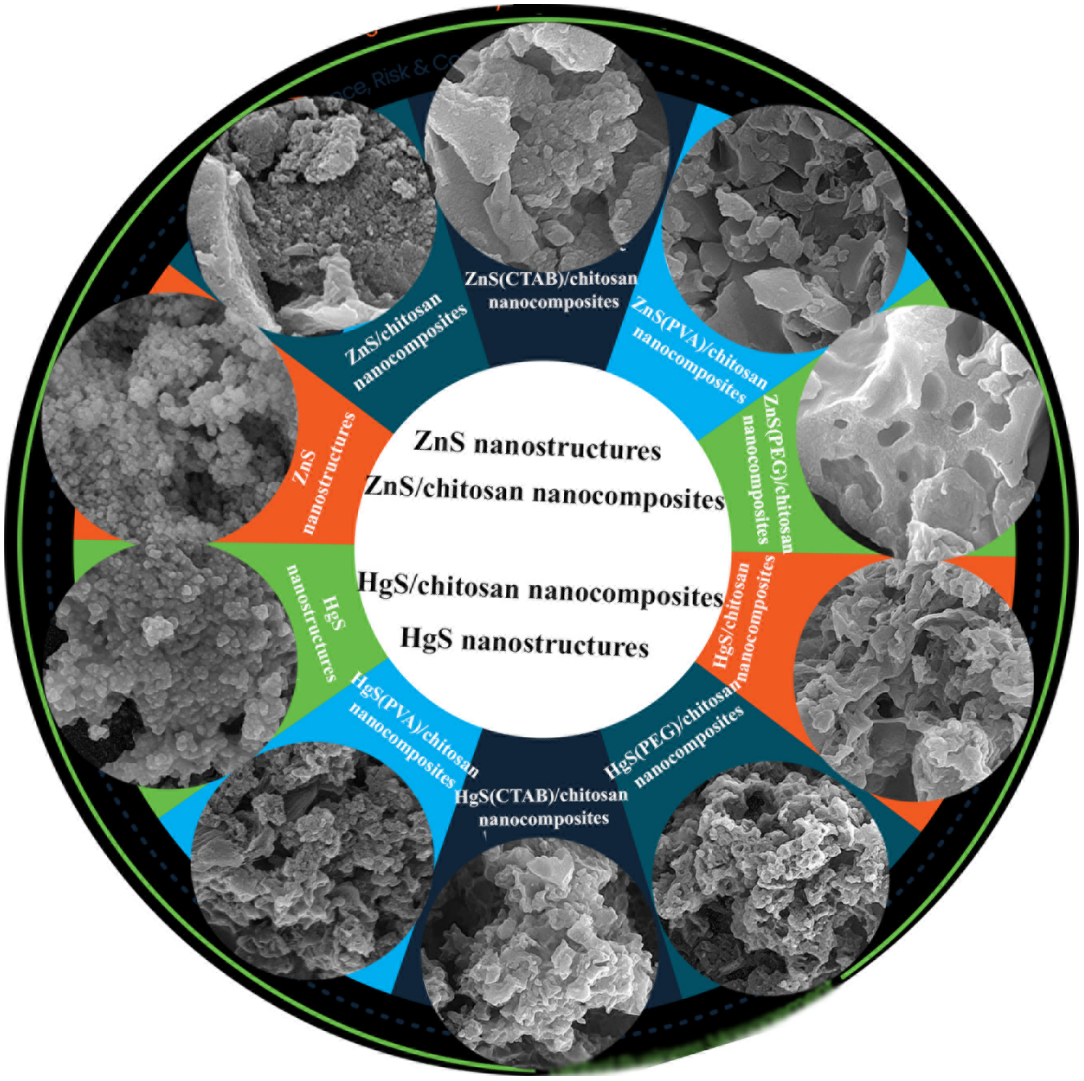

Fig. 7. Schematic diagram for ZnS and HgS NSs and ZnS/Chit and HgS/Chit NCs with SEM images.

nanostructures and nanocomposites as-prepared in this work, have been shown in Fig. 9a. The black curve corresponds to the UV-Vis spectrum of MB and featuring three bands: one in the visible region (~665 nm) and two in the UV region (~300 nm and ~250 nm). As shown in Fig. 9a, the HgS/Chit NC is ineffective as an adsorbent for MB removal, as the UV intensity of MB remains unchanged in its presence. ZnS NSs also show limited adsorption capability, with no significant reduction in the

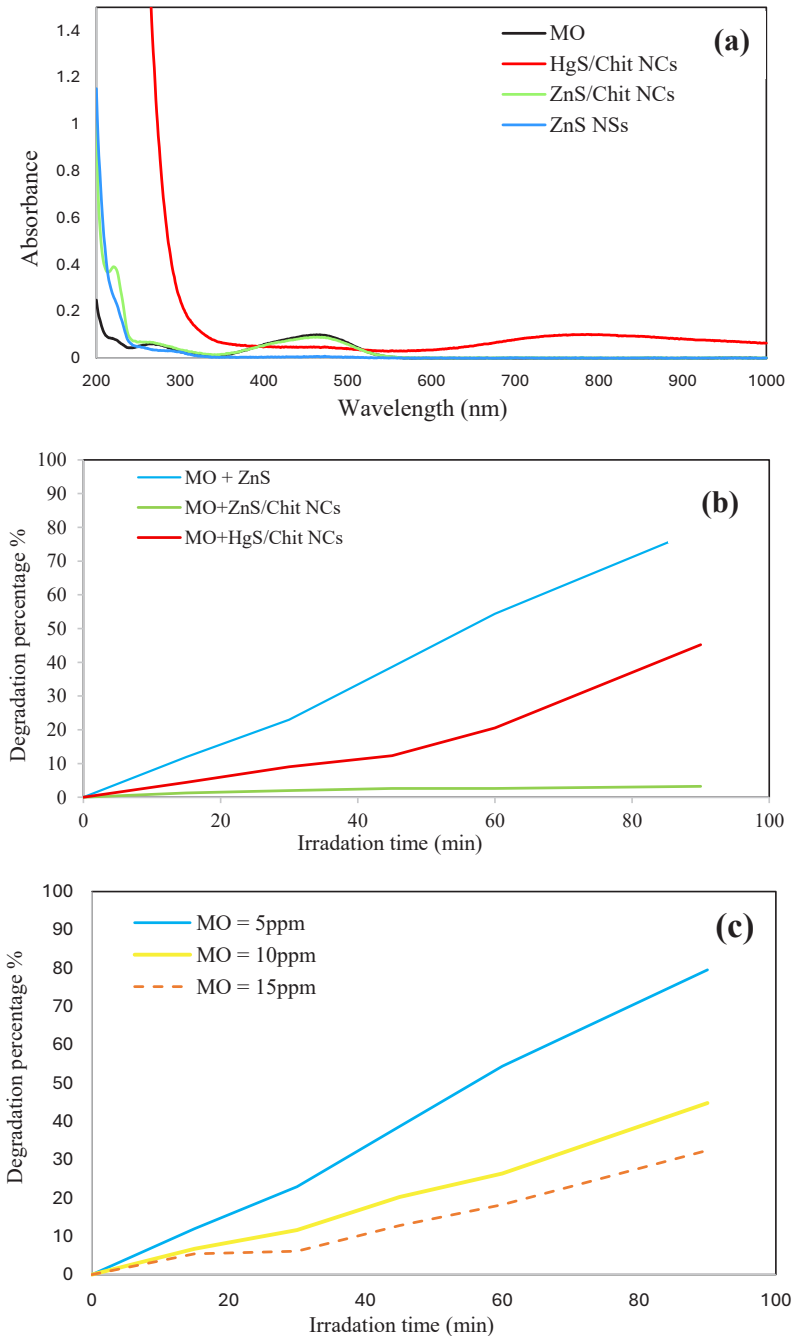

Fig. 8. (a) Absorption spectra of MO and the solutions of MO with ZnS, ZnS/Chit, and HgS/Chit NCs, (b) Photodegradation efficiency of MO in the presence of ZnS, ZnS/Chit, and HgS/Chit NCs, (c) Influence of the dye concentration on photodegradation efficiency of MO.

UV peak intensities of MB. In contrast, the red curve (ZnS/Chit NCs) demonstrates complete elimination of the MB UV-Vis peaks, confirming the high efficacy of this nanocomposite for MB removal. Thus, the absorption spectra results indicate the suitable performance of ZnS/Chit NCs

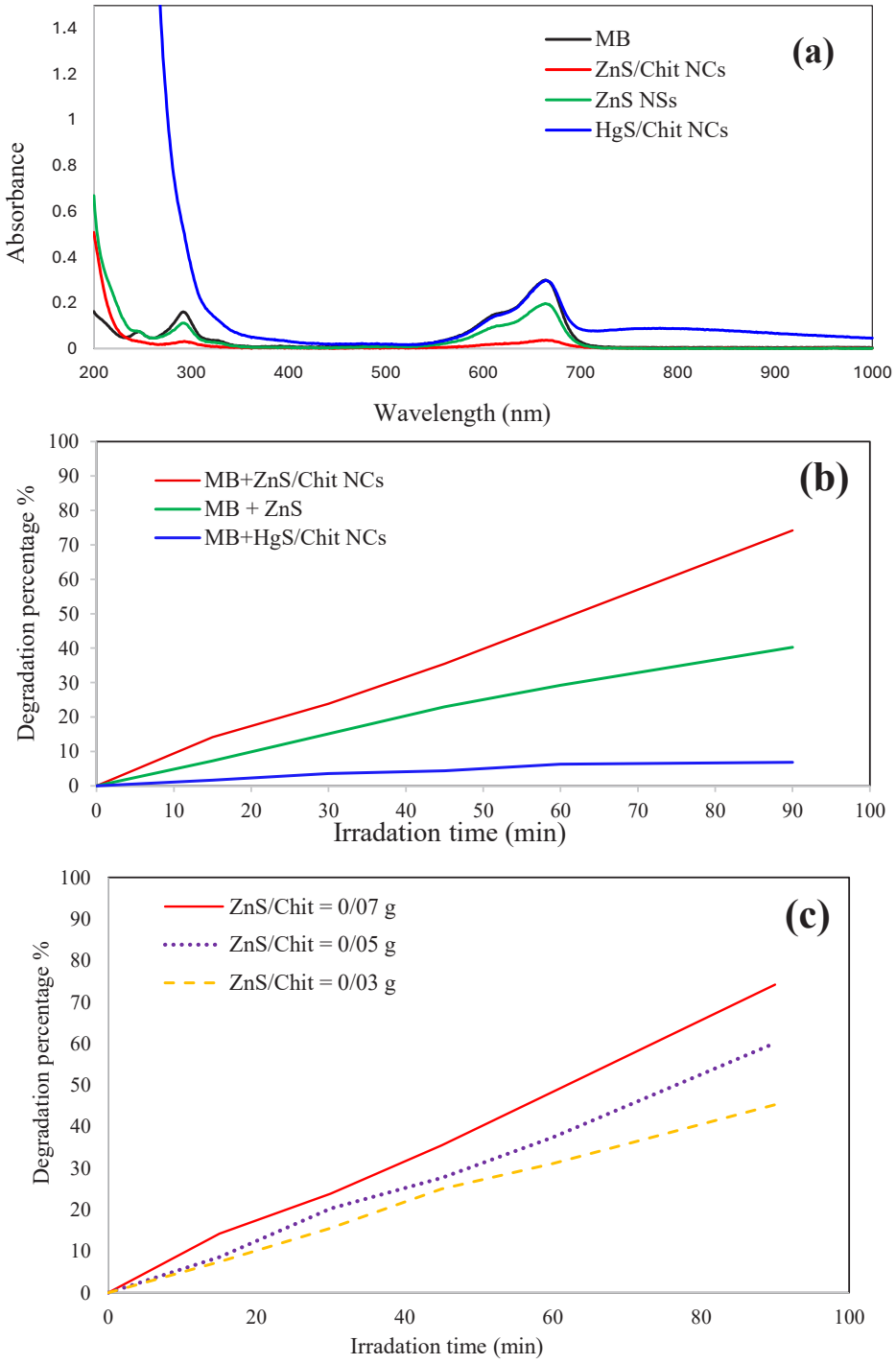

Fig. 9. (a) Absorption spectra of MB and the solutions of MB with ZnS, ZnS/Chit, and HgS/Chit NCs, (b) Photodegradation efficiency of MB in the presence of ZnS, ZnS/Chit, and HgS/Chit NCs, (c) Influence of the photocatalyst content on photodegradation efficiency of MB.

in MB removal. The degradation efficiencies of MB in the presence of ZnS, ZnS/Chit, and HgS/Chit NCs are compared in Fig. 9b, confirming the ZnS/Chit NCs as the most effective photocatalyst. To further explore the photocatalytic performance, the influence of catalyst content was investigated by applying three different contents of the photocatalyst. The results, illustrated in Fig. 9c, reveal the dependence of photocatalytic activity on the catalyst content. An increased amount of catalyst provides more sites for light absorption and facilitates chemical reactions. Consequently, it accelerates the production of reactive oxygen species, such as hydroxyl radicals and superoxide ions. As depicted in Fig. 9c, enhancing the catalyst amount from 0/03 g to 0/07 g led to a more effective photodegradation process. A higher quantity of catalyst distributed over a larger area result in more colored substances adhering to the surface of ZnS/Chit NCs.

CONCLUSION

In this study, MS/Chit NCs were obtained through a three-step simple method, including reflux, thermal decomposition and stirring. The different surfactants were used and their effects investigated. The nanocomposites were characterized via XRD, SEM, EDS and FT-IR. The successfully synthesized ZnS and ZnS/Chit NC were used to remove MO and MB from water, respectively. The highest degradation efficiencies of ZnS and ZnS/Chit NCs with MO and MB were reported as 79% and 74% under UV irradiation after 90 min, respectively.

ACKNOWLEDGEMENTS

The study was supported by Kosar University of Bojnord.

CONFLICT OF INTEREST

The authors declare that there is no conflict of interests regarding the publication of this manuscript.

REFERENCES

1. Sobhani A, Salavati-Niasari M, Sobhani M. Synthesis, characterization and optical properties of mercury sulfides and zinc sulfides using single-source precursor. Mater Sci Semicond Process. 2013;16(2):410-417.
2. Regmi A, Bhattarai BR, Gautam SK. Synthesis and Microscopic Study of Zinc Sulfide Nanoparticles. 2019 International Conference on Computer, Communication, Chemical, Materials and Electronic Engineering (IC4ME2); 2019/07: IEEE; 2019. p. 1-4.
3. Wei S, Zheng Q. Biosynthesis and characterization of zinc sulphide nanoparticles produced by the bacterium Lysinibacillus sp. SH74. Ceram Int. 2024;50(2):2637-2642.
4. Zhang H, Yong K-T, Swihart MT. Synthesis of Zinc Sulfide Nanoparticles by Spray Pyrolysis. ECS Transactions. 2007;2(7):249-254.
5. Ho S. Recent advancement in the synthesis of zinc sulphide thin films. Research Journal of Chemistry and Environment. 2024;28(6):87-100.
6. Srinivasan N, Thirumaran S, Ciattini S. Synthesis of α-mercury sulfide nanosheets from (1,10-phenanthroline)bis(1,2,3,4-tetrahydroquinolinecarbodithioato-S,S')mercury(II). J Mol Struct. 2014;1076:382-386.
7. Seyghalkar H, Sabet M, Salavati-Niasari M. Synthesis and Characterization of Cadmium Sulfide Nanoparticles via a Simple Thermal Decompose Method. nano Online: De Gruyter; 2017.
8. Stadnik V, Guminilovych R, Sozanskyi M, Shapoval P, Deva L. Hydrochemical Synthesis and Properties of Mercury Sulfide (HgS) and Mercury Selenide (HgSe) Thin Films. MDPI AG; 2023.
9. Kristl M, Drofenik M. Sonochemical synthesis of nanocrystalline mercury sulfide, selenide and telluride in aqueous solutions. Ultrason Sonochem. 2008;15(5):695-699.
10. Kuno J, Miyake K, Katao S, Kawai T, Nakashima T. Enhanced Enantioselectivity in the Synthesis of Mercury Sulfide Nanoparticles through Ostwald Ripening. Chem Mater. 2020;32(19):8412-8419.
11. Wichiansee W, Nordin MN, Green M, Curry RJ. Synthesis and optical characterization of infra-red emitting mercury sulfide (HgS) quantum dots. J Mater Chem. 2011;21(20):7331.
12. Rahmatolahzadeh R, Mousavi-Kamazani M, Shobeiri SA. Facile Co-precipitation-calcination Synthesis of $CuCo_2O_4$ Nanostructures using Novel Precursors for Degradation of Azo Dyes. Journal of Inorganic and Organometallic Polymers and Materials. 2016;27(1):313-322.
13. Beshkar F, Al-Nayili A, Amiri O, Salavati-Niasari M, Mousavi-Kamazani M. Fabrication of S-scheme $ZnO/Zn_3(PO_4)_2$ heterojunction photocatalyst toward photodegradation of tetracycline antibiotic and photocatalytic mechanism insight. Int J Hydrogen Energy. 2022;47(2):928-939.
14. Mousavi-Kamazani M. Facile hydrothermal synthesis of egg-like $BiVO_4$ nanostructures for photocatalytic desulfurization of thiophene under visible light irradiation. Journal of Materials Science: Materials in Electronics. 2019;30(19):17735-17740.
15. Masoumi S, Nabiyouni G, Ghanbari D. Photo-degradation of azo dyes: photo catalyst and magnetic investigation of $CuFe_2O_4$–TiO_2 nanoparticles and nanocomposites. Journal of Materials Science: Materials in Electronics. 2016;27(9):9962-9975.
16. Zinatloo-Ajabshir S, Morassaei MS, Amiri O, Salavati-Niasari M. Green synthesis of dysprosium stannate nanoparticles using Ficus carica extract as photocatalyst for the degradation of organic pollutants under visible irradiation. Ceram Int. 2020;46(5):6095-6107.
17. Zinatloo-Ajabshir S, Morassaei MS, Salavati-Niasari M. Eco-friendly synthesis of $Nd_2Sn_2O_7$–based nanostructure materials using grape juice as green fuel as photocatalyst for the degradation of erythrosine. Composites Part B: Engineering. 2019;167:643-653.

18. Zinatloo-Ajabshir S, Salavati-Niasari M. Preparation of magnetically retrievable $CoFe_2O_4$@SiO_2@$Dy_2Ce_2O_7$ nanocomposites as novel photocatalyst for highly efficient degradation of organic contaminants. Composites Part B: Engineering. 2019;174:106930.
19. Samadi Kazemi M, Sobhani A. $CuMn_2O_4$/chitosan micro/nanocomposite: Green synthesis, methylene blue removal, and study of kinetic adsorption, adsorption isotherm experiments, mechanism and adsorbent capacity. Arabian Journal of Chemistry. 2023;16(6):104754.
20. Wang C, Yin L, Xu Z, Niu J, Hou L-A. Electrochemical degradation of enrofloxacin by lead dioxide anode: Kinetics, mechanism and toxicity evaluation. Chem Eng J. 2017;326:911-920.
21. Zinatloo-Ajabshir S, Morassaei MS, Amiri O, Salavati-Niasari M, Foong LK. $Nd_2Sn_2O_7$ nanostructures: Green synthesis and characterization using date palm extract, a potential electrochemical hydrogen storage material. Ceram Int. 2020;46(11):17186-17196.
22. Bayat S, Sobhani A, Salavati-Niasari M. Co_2SiO_4 nanostructures/nanocomposites: synthesis and investigations of optical, magnetic, photocatalytic, thermal stability and flame retardant properties. Journal of Materials Science: Materials in Electronics. 2018;29(9):7077-7089.
23. Mohassel R, Sobhani A, Salavati-Niasari M, Goudarzi M. Pechini synthesis and characteristics of Gd_2CoMnO_6 nanostructures and its structural, optical and photocatalytic properties. Spectrochimica Acta Part A: Molecular and Biomolecular Spectroscopy. 2018;204:232-240.
24. Shahrokhian S, Jokar E, Ghalkhani M. Electrochemical determination of piroxicam on the surface of pyrolytic graphite electrode modified with a film of carbon nanoparticle-chitosan. Microchimica Acta. 2010;170(1-2):141-146.
25. Sharma K, Somavarapu S, Colombani A, Govind N, Taylor KMG. Crosslinked chitosan nanoparticle formulations for delivery from pressurized metered dose inhalers. Eur J Pharm Biopharm. 2012;81(1):74-81.
26. Agnihotri SA, Mallikarjuna NN, Aminabhavi TM. Recent advances on chitosan-based micro- and nanoparticles in drug delivery. Journal of Controlled Release. 2004;100(1):5-28.
27. Hirota Y, Tominaga T, Kawabata T, Kawakita Y, Matsuo Y. Hydrogen Dynamics in Hydrated Chitosan by Quasi-Elastic Neutron Scattering. Bioengineering. 2022;9(10):599.
28. Ghiyasiyan-Arani M, Salavati-Niasari M, Naseh S. Enhanced photodegradation of dye in waste water using iron vanadate nanocomposite; ultrasound-assisted preparation and characterization. Ultrason Sonochem. 2017;39:494-503.
29. Karimi Anjiraki M, Ghiyasiyan-Arani M, Baladi M, Alsultany FH, Shabani-Nooshabadi M, Salavati-Niasari M. Magnetically recyclable $PrFeO_3$/g-C_3N_4 nano-photocatalyst with Z-scheme structure: Synthesis and characterization and its application for enhanced degradation of malachite green as contaminated water under sunlight. Inorg Chem Commun. 2024;170:113184.
30. Review for "Synthesis and Modification of UiO-66(Ce) for Adsorptive Removal of Methylene Blue and Cu(II) Ions". Royal Society of Chemistry (RSC); 2026.
31. Karimi Anjiraki M, Ghiyasiyan-Arani M, Falah Khudair Z, Baladi M, Shabani-Nooshabadi M, Salavati-Niasari M. A highly efficient $PrMnO_3$/graphene oxide nanocomposite for visible light induced photocatalytic water treatment. Solar Energy. 2024;275:112615.
32. Samimi F, Ghiyasiyan-Arani M. $Zn_2Mo_3O_8$/$ZnMo_8O_{10}$/Mo_8O_{23} nanocomposites; structural properties, synthesis and its emerging application in electrochemical hydrogen storage. Int J Hydrogen Energy. 2024;91:423-433.
33. Qin H, Wang CM, Dong QQ, Zhang L, Zhang X, Ma ZY, et al. Preparation and characterization of magnetic Fe_3O_4–chitosan nanoparticles loaded with isoniazid. J Magn Magn Mater. 2015;381:120-126.